Experimental evaluation of self-sputtering yields and comparison with TRIDYN simulations

M. Deseyn[1⋆] and M. Heines[1]
B. Caerts[2], T.E. Cocolios[1], R. Heller[3], U. Kentsch[3], G. Magchiels[2], W. Möller[3], L. M. C. Pereira[2], A. Vantomme[2], W. Wojtaczka[1] and Q. Zhao[2]

1 Insituut voor Kern- en Stralingsfysica, KU Leuven, Leuven, Belgium
2 Quantum Solid State Physics, KU Leuven, Leuven, Belgium
3 Helmholtz-Zentrum Dresden-Rossendorf, Instituut of Ion Beam Physics and Materials Research, Dresden, Germany

⋆ corresponding author: marie.deseyn@kuleuven

Abstract

In the case of high-fluence implantations, the approximation that every new incoming particle interacts with a pristine substrate material no longer holds. Dynamical changes to the substrate can induce different phenomena, one of which is self-sputtering. Self-sputtering occurs when incoming ions remove previously implanted ions from the implantation substrate. This phenomenon is significant in target production for nuclear structure studies and medical radionuclide separation, where self-sputtering limits can be reached during isotope implantation. Self-sputtering can be modeled using TRIDYN simulations in order to guide implantations. This work explores the ability of TRIDYN to give order-of-magnitude estimates for the onset of self-sputtering for these nuclear physics applications. This is performed through the implantation of Yb in Zn and Al, relevant to both fundamental and medical nuclear physics research. Our findings indicate that TRIDYN predicts general dependencies reasonably well. However, it is important to carefully consider input parameters and validity of the TRIDYN simulations.

Received Date
Accepted Date
Published Date

Introduction

High-fluence effects in ion beam implantation have become increasingly significant in various branches of research. In the field of medical radionuclide production via radioactive ion mass separation and implantation, several isotope collections have shown limitations due to sputtering effects [1]. More specifically, due to self-sputtering, earlier implanted nuclides are removed from the foil upon implanting more nuclei until, eventually, the amount of nuclei of interest in the foil no longer increases. To address this issue, the MEDICIS facility at CERN (Medical Isotopes Collected from ISOLDE) [2] switched the implantation material from zinc to aluminum to mitigate self-sputtering on the premise that the effect would be less pronounced when using a substrate with a lower atomic number. Additionally, self-sputtering effects can be reduced by implementing beam sweeping in order to increase the implantation area and consequently reduce the fluence for the same amount of total collected ions. However, scaling up

production to meet the growing demand for radionuclides necessitates careful consideration of sputtering. In fundamental nuclear physics research, several experiments, such as muonic atom spectroscopy [3] and neutron time-of-flight studies [4], require $\mathcal{O}(1-100)\,\mu$g of target material onto surfaces of $\mathcal{O}(1)\,\mathrm{cm}^2$. Preparing such targets through implantation necessitates operating within the range where self-sputtering plays a significant role. Despite the diverse interests of these nuclear physics research fields, they share a common goal: implanting a large number of particles on a small surface area without significant loss due to sputtering.

Many simulations in the scope of implantations are performed using SRIM [5]. This software is a Monte Carlo-based simulation package that models implantation processes through the binary collision approximation. While SRIM provides sufficiently reliable estimates for most applications, it only considers a static pristine sample. However, when dynamical effects become important, the validity of SRIM breaks down. TRIDYN [6] is built around the same framework as SRIM, but allows for dynamic simulations, such as self-sputtering. Additionally, different implantation conditions can be applied either simultaneously or sequentially through layered simulations. These simulations can predict the retained fluence (number of particles per unit area) as a function of the incoming fluence, helping to determine the optimal stopping point for implantation and/or when to switch to a new sample.

Experimental validation of these simulations is sparse due to the long machine times required for high-fluence implantations [7, 8]. However, the need for systematic investigations became apparent during single implantations for both muonic atom research (gold implantations) [9] and implantations for medical applications at MEDICIS [10]. In both cases, clear signs of self-sputtering were observed [1, 9], which motivated a thorough investigation of retained fluence curves and a subsequent comparison with corresponding simulation results. In this work, the implantation of ytterbium (Yb, as a proxy for all lanthanides) into aluminum (Al) and zinc (Zn) was investigated and compared to the TRIDYN simulations.

1 Methods

1.1 TRIDYN

Simulations of the ion implantations were performed using TRIDYN version 2022 [6] (most recent version at the time of writing). Key parameters for the simulations include the initial target composition and thickness, the total implanted fluence, irradiation conditions, and the surface binding energy matrix. A general description of these parameters can be found in Ref. [11]. Among these parameters, we direct our focus towards the surface binding energy, as it plays a crucial role in the systematic study that was performed. For this, we employ the zero bulk binding energy approximation, as recommended for TRIDYN [12].

The surface binding energy matrix of a material ($\mathrm{X_nY_m}$) is given by

$$sbe = \begin{pmatrix} SBE_{\mathrm{Y\text{-}Y}} & SBE_{\mathrm{Y\text{-}X}} \\ SBE_{\mathrm{X\text{-}Y}} & SBE_{\mathrm{X\text{-}X}} \end{pmatrix}. \tag{1}$$

These matrix elements represent the interaction energies between materials X and Y and are crucial in quantifying the sputtering behavior. Specifically, they quantify the contributions from phenomena such as sublimation, formation, and dissociation of the compounds, which determine the bonding behavior at the surface.

The surface binding energy values are modeled depending on the phase of matter of the involved compounds; $\mathrm{SBE_{X\text{-}X}}$ is assumed to be 0 eV for gases and equal to the sublimation enthalpy (ΔH^s) in solids. For X a solid and Y a gas with molecular fractions n and m, respectively,

X	ΔH_X^s	Ref.
C	4.5 eV	[13]
Au	3.8 eV	[11]
Al	3.36 eV	[14]
Yb	1.74 eV	[11]
K	0.93 eV	[11]
XY	ΔH_{XY}^f	**Ref.**
AuC	1.03 eV	[15]
Al_2O_3	3.36 eV	[14]
Yb_2O_3	3.36 eV	[14]
$YbAl_2$	0.7588 eV	[16]
YbZn	0.338 eV	[17, 18]
Y	ΔH_Y^{diss}	**Ref.**
O_2	5.16 eV	[14]

Table 1: Overview of the used sublimation and formation enthalpies as well as the dissociation energy used in this work.

the matrix element, $SBE_{X\text{-}Y}$, is calculated as [11]

$$SBE_{X\text{-}Y} = \frac{1}{2}\Delta H_X^s + \frac{n+m}{2nm}\Delta H_{XY}^f + \frac{n+m}{4n}\Delta H_Y^{diss},$$

with ΔH_X^s the sublimation enthalpy, ΔH^f the formation enthalpy per molecule of the compound and ΔH^{diss} the dissociation energy of the gas molecule Y [11]. For two solids with molecular fractions n and m, the surface binding energy matrix element is given by [11]:

$$SBE_{X\text{-}Y} = \frac{\Delta H_X^s + \Delta H_Y^s}{2} + \frac{n+m}{2mn}\Delta H_{XY}^f. \tag{2}$$

A summary of the sublimation enthalpies, formation enthalpies and dissociation energy used in the remainder of this work is given in Table 1.

1.2 Experiments

Vacuum during implantation [mbar]	$2.5 \cdot 10^{-6}$
Current density [μA/cm^2]	0.08
Ion energy [keV]	60

Table 2: Experimental implantation conditions

The samples used for this work were implanted at the High Current Ion Implanter in the Ion and Molecular Beam Laboratory (IMBL) at KU Leuven [19]. To achieve a uniform fluence profile, beam sweeping was applied during implantation. Small samples, approximately 5 mm × 5 mm, were implanted with varying incoming fluences. A summary of the implantation conditions is provided in Table 2.

To optimize machine time, multiple samples were implanted simultaneously (see Appendix A for the detailed implantation scheme). After the implantations, Rutherford backscattering spectrometry (RBS) was performed on site to characterize the samples. Besides identifying the elements, RBS provides information about the absolute number of particles of a specific species per unit area. The number of particles per unit area of a certain element is (in first order)

proportional to the integral of its corresponding peak in the spectrum. Hence the retained fluence (ψ_{retained}) in the foils can be determined using

$$\psi_{\text{retained}} = \psi_{\text{cal}} \frac{I_{\text{RBS}}}{I_{\text{cal}}} \frac{Q_T(\text{cal})}{Q_T(\text{exp})}. \tag{3}$$

Here, ψ_{cal} corresponds to the fluence calculated from the peak of interest simulated in the calibration spectrum (RBS on $AuCo_3/SiO_2/Si$, using SIMNRA [20]). I_{cal} and I_{RBS} are the integrals over the peak of interest in the simulated peak from the calibration measurement and measurement of the implanted samples, respectively. Lastly, $Q_T(\text{cal})$ and $Q_T(\text{exp})$ correspond to the total collected charge on the substrate during the calibration measurement and sample measurement, respectively.

2 Results

For investigation of self-sputtering in the lanthanide region, implantations of Yb in Al and Zn were performed at 60keV for implantation fluences ranging from $0.26\,\text{Å}^{-2}$ to $6.0\,\text{Å}^{-2}$. For each set of these implantations, two different TRIDYN simulations were performed. The first simulation models implantation in bulk Al_2O_3 or ZnO, while the second models implantation in bulk Al or Zn with a layer of Al_2O_3 or ZnO on top. The thickness of this layer is determined from the thickness of the native layer, given by 3.0 nm [21] and 1.5 nm [22] for Al_2O_3 and ZnO, respectively. The surface binding energy for implantation of Yb in Al_2O_3 was determined using the values in Table 1 as follows:

$$\begin{aligned} sbe_{\text{Al}} &= \begin{pmatrix} SBE_{\text{Yb-Yb}} & SBE_{\text{Yb-Al}} & SBE_{\text{Yb-O}} \\ SBE_{\text{Al-Yb}} & SBE_{\text{Al-Al}} & SBE_{\text{Al-O}} \\ SBE_{\text{O-Yb}} & SBE_{\text{O-Al}} & SBE_{\text{O-O}} \end{pmatrix} \\ &= \begin{pmatrix} 1.74\,\text{eV} & 3.1191\,\text{eV} & 11.93\,\text{eV} \\ 3.1191\,\text{eV} & 3.36\,\text{eV} & 12.155\,\text{eV} \\ 11.93\,\text{eV} & 12.155\,\text{eV} & 0\,\text{eV} \end{pmatrix}. \end{aligned} \tag{4}$$

Similarly, the surface binding energy matrix for implantation of Yb in ZnO is given by:

$$\begin{aligned} sbe_{\text{Zn}} &= \begin{pmatrix} SBE_{\text{Yb-Yb}} & SBE_{\text{Yb-Zn}} & SBE_{\text{Yb-O}} \\ SBE_{\text{Zn-Yb}} & SBE_{\text{Zn-Zn}} & SBE_{\text{Zn-O}} \\ SBE_{\text{O-Yb}} & SBE_{\text{O-Zn}} & SBE_{\text{O-O}} \end{pmatrix} \\ &= \begin{pmatrix} 1.74\,\text{eV} & 1.883\,\text{eV} & 11.93\,\text{eV} \\ 1.883\,\text{eV} & 1.35\,\text{eV} & 6.885\,\text{eV} \\ 11.93\,\text{eV} & 6.885\,\text{eV} & 0\,\text{eV} \end{pmatrix}. \end{aligned} \tag{5}$$

The corresponding experimental results, inferred from the RBS spectra, as well as the simulation results are shown in Figure 1 and 2.

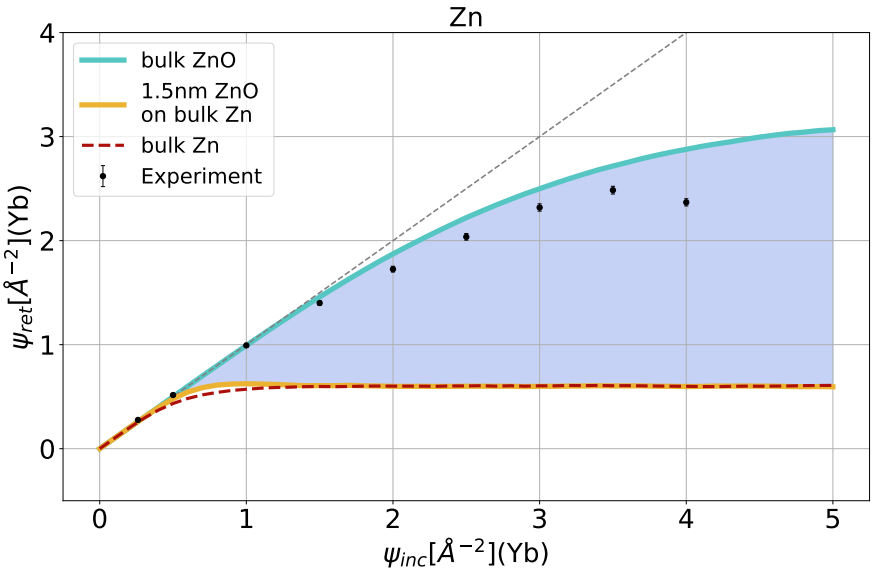

Figure 1: Experimental data for the retained fluence (ψ_{ret}) as a function of the incoming fluence (ψ_{inc}) compared to the simulation of bulk ZnO and the simulation of bulk Zn with a native layer of 1.5nm ZnO on top. For reference, the simulation for implantation in bulk Zn is shown in red (dashed).

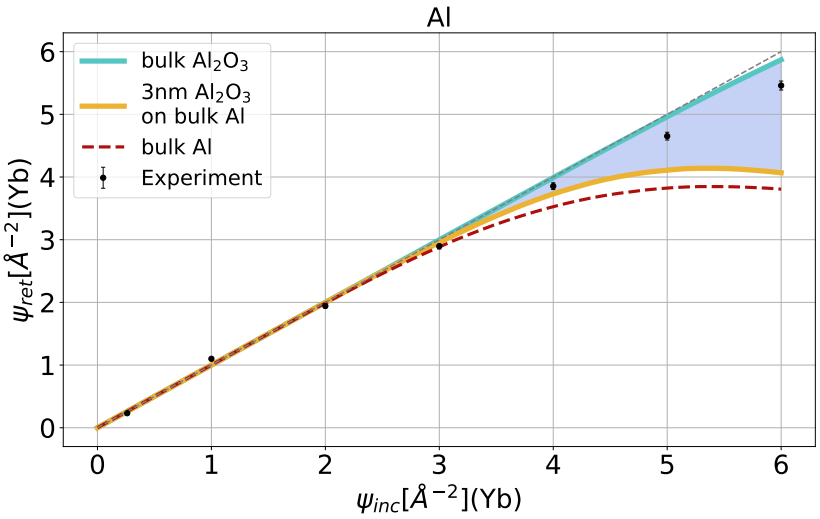

Figure 2: Experimental data for the retained fluence (ψ_{ret}) as a function of the incoming fluence (ψ_{inc}) compared to the simulation of bulk Al_2O_3 and the simulation of bulk Al with a native layer of 3nm Al_2O_3 on top. For reference, the simulation for implantation in bulk Al is shown in red (dashed).

From comparison of these simulations with the experimental data, it is concluded that the bulk oxide simulations and the native layer simulations provide an upper and lower boundary for the experimental data, respectively. This can be explained through the implantation procedure which started from a bulk Al (Zn) plate with a native layer of Al_2O_3 (ZnO). Subsequently, ytterbium is implanted and part of the oxygen is sputtered from the foil, which

gradually increases the Z-value of the foil as well as the self-sputtering yield. After the first implantation step, all foils are extracted from the vacuum to remove the first foil. At this point, a new native oxide layer is formed prior to the next Yb implantation step. As such, the oxide layer systematically rebuilds upon removal from the vacuum. Due to the lower Z of oxygen compared to aluminum and zinc, self-sputtering is reduced. As a result, the experimental retained fluence is larger than the simulation of a bulk Al (Zn) plate with a native layer of Al_2O_3 (ZnO) foil on top. On the other hand, the native thickness of the oxygen layer that is rebuilt is considerably smaller than the implantation depth, thereby decreasing the retained fluence compared to the bulk Al_2O_3 (ZnO) simulations. Furthermore, as illustrated in Figure 3, which shows the retained oxide layer as a function of the incoming Yb fluence, the incoming Yb fluence at which the native oxide layer is sputtered away is of the same order of magnitude as the incoming fluence in one implantation step ($0.25\,\text{Å}^{-2} - 1\,\text{Å}^{-2}$). This is also suggested from a back-of-the-envelope calculation of the thickness of the sputtered layer from a fully oxidized substrate, which equals 1.28 nm and 4.02 nm for implantation of $0.5\,\text{Å}^{-2}$ of Yb in bulk Al_2O_3 and ZnO, respectively (see Appendix B). This indicates that the oxide layer is significantly sputtered away in each implantation step. Subsequently, upon removal of the foils, a combined ytterbium oxide and aluminum oxide (zinc oxide) native layer is reformed. The detailed formation of this combined oxide layer is beyond the scope of this publication.

Note also that the self-sputtering for implantation in Zn is stronger than in Al, because of the higher proton-number of Zn. The full impact of self-sputtering across different implantation foils and implantation materials will be discussed in a subsequent paper, specifically focusing on medically relevant cases.

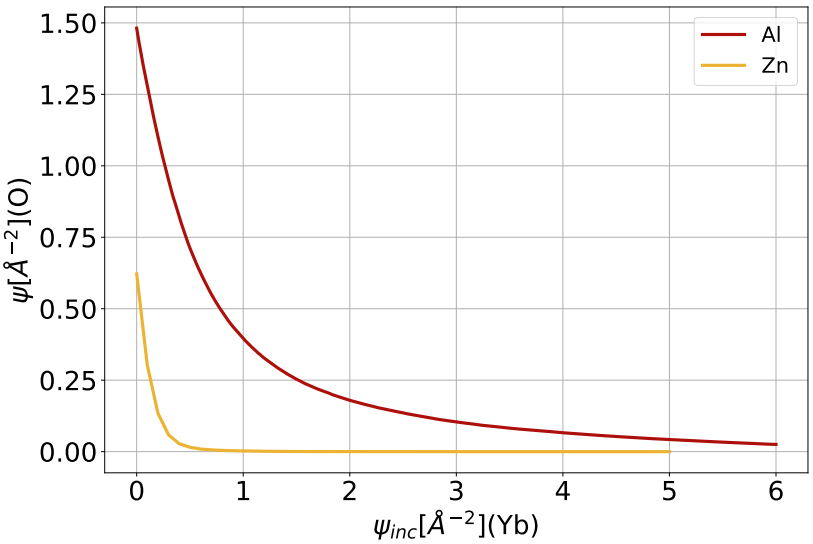

Figure 3: Simulated oxygen fluence in the substrate for implantation of Yb in Al (Zn) with a native layer of Al_2O_3 (ZnO) on top.

Implantation of K and Au in C

In addition to the primary focus on Yb self-sputtering in Zn and Al, implantation experiments with Au and K in C were conducted to assess the limitations of TRIDYN. For Au implanted into glassy carbon, adjustments to the surface binding energy matrix compared to earlier work [9] improved the agreement between simulation and experiment. However, significant discrepancies persist, likely due to substrate porosity and the immiscibility of the Au-C system. Similarly,

K implantation in pyrolytic graphite revealed deviations from TRIDYN predictions, which are attributed to the immiscibility of the K-C system, thermal diffusion, surface oxidation during handling, and material porosity. These results emphasize the limitations of TRIDYN when applied to immiscible systems. Full experimental data and simulation details for these studies are provided in Appendix C.

Conclusion

In this study, we have investigated the performance of TRIDYN in modeling self-sputtering for implantations relevant to the target-making for fundamental nuclear structure studies and medical isotope collections. The retained fluence was measured experimentally for varying implantation fluences and the results were compared to the simulations. Our experimental results indicate that while TRIDYN effectively models the general trends of implantation and sputtering, careful consideration of input parameters is crucial, and the results should be interpreted with caution.

Dynamic changes to the oxide layer between different implantation steps can significantly affect the retained fluence. For potassium and gold, the simulations deviated substantially from the experimental trend, likely due to a combination of the immiscibility, thermal diffusion and the strong reactivity of potassium. These variances suggest that while TRIDYN can serve as a valuable predictive tool, it has limitations.

Acknowledgements

Author contributions B.C., R.H., U.K., G.M. and Q.Z. were involved in the experiment (implantations + RBS). M.D. and M.H. performed the simulations. M.D., M.H., G.M. were involved in the data-analysis and T.E.C., M.D., M.H., W.M., L.P., A.V. and W.W. were involved in the discussion of the results. M.H. and M.D. wrote the manuscript and all co-authors reviewed it. We would also like to thank K. van Stiphout for the valuable discussions.

Funding information This work received funding from FWO Vlaanderen (S005019N, G0G3121N), KU Leuven BOF (C14/22/104), and from the European Commission's Horizon 2020 INFRA (RADIATE no. 824096). M.D. was supported by an FWO Aspirant Fundamental Research (no. 11P6V24N).

A Implantation scheme

Table 3: Presence of foils inside the implanter during each implantation step, in between two implantation steps, the foils were removed from the vacuum. An "×" marks when the foil was present for the corresponding implantation step. The vertical labels, such as "Zn - 2.5" indicate the Zn foil that was implanted up to 2.5 $Å^{-2}$, while the horizontal labels indicate the fluence ($Å^{-2}$) implanted in that specific step.

Foil	0.261	0.239	0.5	0.5	0.5	0.5	0.5	1.0	1.0	0.3	0.7
Zn – 0.5	×	×									
Zn – 1	×	×	×								
Zn – 1.5	×	×	×	×							
Zn – 2	×	×	×	×	×						
Zn – 2.5	×	×	×	×	×	×					
Zn – 3	×	×					×	×	×		
Zn – 3.5	×	×	×				×	×	×		
Zn – 4	×	×	×	×			×	×	×		
Al – 1	×	×	×								
Al – 2	×	×	×	×	×						
Al – 3	×	×	×	×	×	×	×				
Al – 4	×	×	×	×	×	×	×	×			
Al – 5	×	×	×	×	×	×	×	×	×		
Al – 6	×	×	×	×	×	×	×	×	×	×	×

B Calculation of the thickness of the sputtered layer

In this appendix, a back-of-the-envelope calculation to determine the thickness of the sputtered layer from a fully oxidized substrate is presented. These calculations hold under the assumption that the sputtered species leave the foil as molecules, which is a first-order approximation. These calculations rely on the sputtering yield of oxygen, which is outputted by TRIDYN.

B.1 Al

The simulation for implantation in bulk Al_2O_3 shows a sputtering yield for O of $Y_{\text{sputtered, O}} = 1.79$. To calculate what thickness this corresponds to, the molecular density is determined:

$$n_{\text{molecule}} = \frac{\rho N_a}{M} = \frac{3.95\,\frac{\text{g}}{\text{cm}^3} \cdot N_a}{101.96\,\frac{\text{g}}{\text{mol}}} = 2.33 \cdot 10^{-2}\,\frac{\text{molecules}}{\text{Å}^3}. \tag{B.1}$$

Here, ρ is the mass density, N_a is Avogadros constant, and M is the molar mass. Subsequently, the thickness of the sputtered layer (t) can be calculated as:

$$t = \frac{\psi_{\text{sputtered, O}}}{n_{\text{O}}} = \frac{\psi_{\text{inc}} \cdot Y_{\text{sputtered, O}}}{n_{\text{O}}} = \psi_{\text{inc}} \cdot 25.54\,\text{Å}^3. \tag{B.2}$$

Here, $n_{\text{O}} = 3n_{\text{molecule}}$ is the atomic density and ψ_{inc} is the incoming Yb fluence. Hence, for incoming fluences of $0.5\,\text{Å}^{-2}$ and $1\,\text{Å}^{-2}$, the thickness of the sputtered layer equals 12.77 Å and 25.54 Å, respectively.

B.2 Zn

For implantation in bulk ZnO, a sputtering yield for O of $Y_{\text{sputtered, O}} = 3.33$ is found. First, the molecular density is determined:

$$n_{\text{molecule}} = \frac{\rho N_a}{M} = \frac{5.61\,\frac{\text{g}}{\text{cm}^3} \cdot N_a}{81.379\,\frac{\text{g}}{\text{mol}}} = 4.15 \cdot 10^{-2}\,\frac{\text{molecules}}{\text{Å}^3}. \tag{B.3}$$

Now, the thickness of the sputtered layer (t) is calculated as:

$$t = \frac{\psi_{\text{sputtered, O}}}{n_{\text{O}}} = \frac{\psi_{\text{inc}} \cdot Y_{\text{sputtered, O}}}{n_{\text{O}}} = \psi_{\text{inc}} \cdot 80.36\,\text{Å}^3. \tag{B.4}$$

Here, $n_{\text{O}} = n_{\text{molecule}}$ is used. For incoming fluences of $0.5\,\text{Å}^{-2}$ and $1\,\text{Å}^{-2}$, the thickness of the sputtered layer equals 40.18 Å and 80.36 Å, respectively.

C Implantation of K and Au in C

In this section, the experimental results for Au and K implantation in C are presented, combined with a TRIDYN simulation. However, the reliability of TRIDYN for these implantations is limited due to the immiscibility of the involved systems.

C.1 Reassessing Au implantations in C

In [9], TRIDYN simulations have been performed for Au implantation in C. These simulations have since been performed with an updated surface binding energy matrix element for carbon, which deviates from the default value assumed by TRIDYN.

$$\begin{aligned} sbe &= \begin{pmatrix} SBE_{\text{C-C}} & SBE_{\text{C-Au}} \\ SBE_{\text{Au-C}} & SBE_{\text{Au-Au}} \end{pmatrix} \\ &= \begin{pmatrix} 4.5\,\text{eV} & 5.18\,\text{eV} \\ 5.18\,\text{eV} & 3.8\,\text{eV} \end{pmatrix}. \end{aligned} \tag{C.1}$$

Here, the values from Table 1 were used. By properly assigning the off-diagonal elements in the binding energy matrix, better agreement was achieved with the experimental data, as

illustrated in Figure 4. Despite this improvement, a significant deviation with the experimental data remains for the 90 keV implantation, which can likely be attributed to the porosity of glassy carbon [9] and/or the immiscibility of the Au-C system resulting in a limited reliability of the TRIDYN simulations.

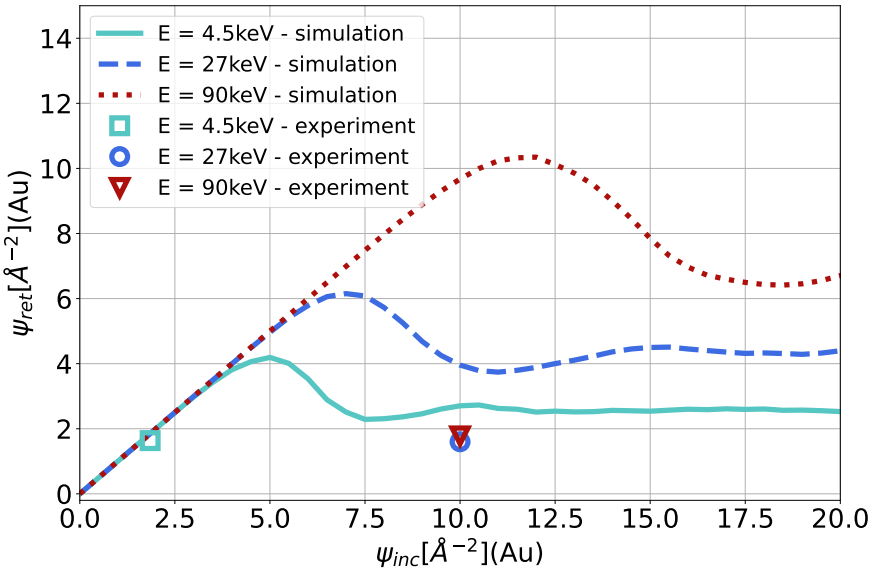

Figure 4: Experimental datapoints for the retained fluence (ψ_{ret}) as a function of the incoming fluence (ψ_{inc}) compared to the simulation for gold implantations in glassy carbon at different energies.

C.2 K implantation in C

These implantations were performed at the 40 kV Ion Implanter at Helmholtz Zentrum Dresden Rossendorf (HZDR) [23]. A beam energy of 30 keV was used with fluences ranging from 5 to 50 $Å^{-2}$. The surface binding energy matrix used for the simulations was calculated to be:

$$sbe = \begin{pmatrix} SBE_{\text{C-C}} & SBE_{\text{C-K}} \\ SBE_{\text{K-C}} & SBE_{\text{K-K}} \end{pmatrix} = \begin{pmatrix} 4.5\,\text{eV} & 2.715\,\text{eV} \\ 2.715\,\text{eV} & 0.93\,\text{eV} \end{pmatrix}. \tag{C.2}$$

For $SBE_{\text{K-C}}$, the ΔH^f term was neglected as no consistent literature value is available, while the other enthalpies and energies are available in Table 1. Figure 5 shows a comparison between the experimental results and the simulations. While the general trend is reproduced, it seems that the maximal retained fluence is nearly a factor two lower than the simulations.

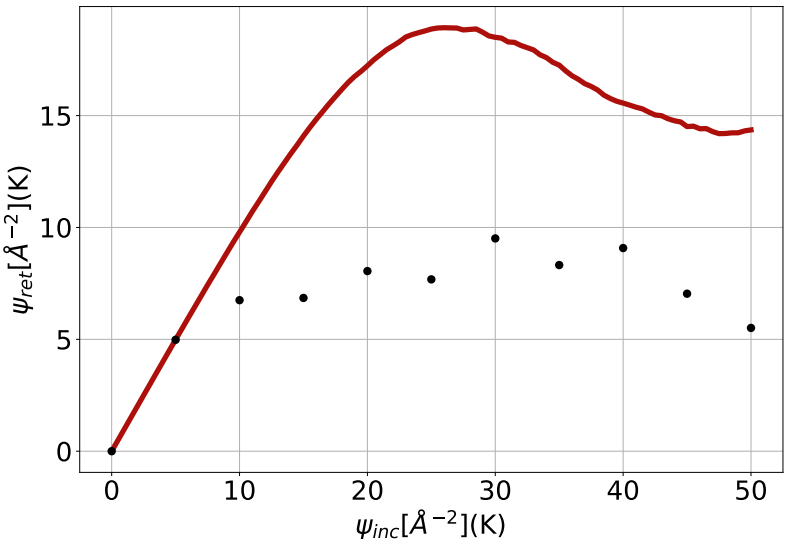

Figure 5: Experimental datapoints for the retained fluence (ψ_{ret}) as a function of the incoming fluence (ψ_{inc}) compared to a TRIDYN simulation for 30 keV ^{39}K in pyrolytic graphite.

The RBS spectrum, shown in Figure 6, gives an indication of two potential causes of this discrepancy. First, the potassium peak has a long low-energy tail, indicating that the distribution of potassium extends deep into the material. This is likely caused by thermal diffusion and/or the high reactivity of elemental potassium, which may be affected by the porosity of the substrate material. Second, a large oxygen peak is present, closely mirroring the structure in potassium. Similar to the ytterbium implantations, we suspect that this oxygen most likely enters the substrate between implantation steps, where the samples are taken out of the vacuum. This may lead to a changing surface binding energy, and hence, changes in the retained fluence curve. Both of these aspects limit the conclusions that can be drawn from these experimental tests with potassium. The pristine sample shows some oxygen in the sample, though substantially less than in the implanted sample. Additionally, a minor background can be seen above 600 keV, though not enough to explain the low energy tail visible in the implanted sample. A simulation for implantation in CO was also performed but did not show significant changes.

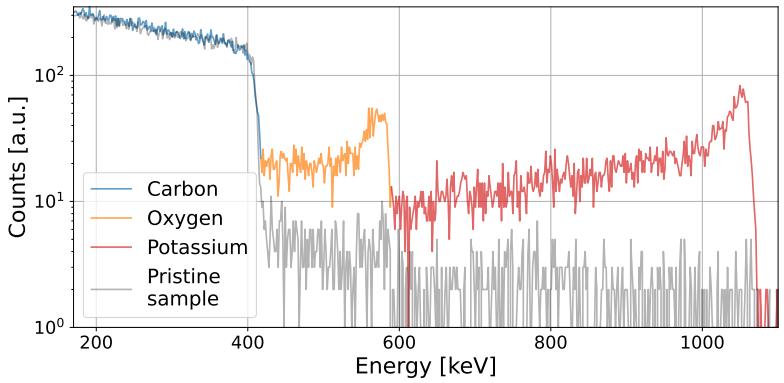

Figure 6: RBS spectrum for a pristine pyrolytic graphite sample (grey) and implanted ^{39}K target (color). The spectrum was obtained using an incident 1.57 MeV ^{4}He$^+$ beam and a detector placed at a scattering angle of 162°.

References

[1] R. Heinke *et al.*, *Efficient production of high specific activity thulium-167 at Paul Scherrer Institute and CERN-MEDICIS*, Frontiers in medicine **8** (2021), doi:10.3389/fmed.2021.712374.

[2] Y. Martinez Palenzuela, *Characterization and optimization of a versatile laser and electron-impact ion source for radioactive ion beam production at ISOLDE and MEDICIS*, Ph.D. thesis, KU Leuven, CDS: https://cds.cern.ch/record/2672954?ln=en (2019).

[3] A. Adamczak *et al.*, *Muonic atom spectroscopy with microgram target material*, The European Physical Journal A **59**(2), 15 (2023), doi:10.48550/arXiv.2209.14365.

[4] C. Lederer-Woods *et al.*, *Destruction of the cosmic γ-ray emitter Al 26 in massive stars: Study of the key Al 26 (n, p) reaction*, Physical Review C **104**(2) (2021), doi:10.1103/PhysRevC.104.L022803.

[5] J. F. Ziegler *et al.*, *SRIM–The stopping and range of ions in matter (2010)*, Nuclear Instruments and Methods in Physics Research Section B: Beam Interactions with Materials and Atoms **268**(11-12), 1818 (2010), doi:10.1016/j.nimb.2010.02.091.

[6] W. Möller and W. Eckstein, *Tridyn—A TRIM simulation code including dynamic composition changes*, Nuclear Instruments and Methods in Physics Research Section B: Beam Interactions with Materials and Atoms **2**(1-3), 814 (1984), doi:10.1016/0168-583X(84)90321-5.

[7] J. Roth *et al.*, *Formation and erosion of WC under W+ irradiation of graphite*, MRS Online Proceedings Library **658**, 5311 (2000), doi:10.1557/PROC-658-O5.31.

[8] H. Hofsäss, F. Junge, P. Kirscht and K. van Stiphout, *Low energy ion-solid interactions: A quantitative experimental verification of binary collision approximation simulations*, Materials Research Express **10**(7) (2023), doi:10.1088/2053-1591/ace41c.

[9] M. Heines *et al.*, *Muonic x-ray spectroscopy on implanted targets*, Nuclear Instruments and Methods in Physics Research Section B: Beam Interactions with Materials and Atoms **541**, 173 (2023), doi:10.1016/j.nimb.2023.05.036.

[10] M. Deseyn, *Maximizing the radionuclide collection efficiency at CERN-MEDICIS: A case study on terbium collections and sputtering*, Master's thesis, KU Leuven, doi:http://cds.cern.ch/record/2866125?ln=en (2023).

[11] W. Möller, *TRIDYN FZR user guide*, https://www.hzdr.de/FWI/FWIT/FILES/Manual_TRIDYN_FZR.pdf (2001).

[12] H. Hofsäss and A. Stegmaier, *Binary collision approximation simulations of ion solid interaction without the concept of surface binding energies*, Nuclear Instruments and Methods in Physics Research Section B: Beam Interactions with Materials and Atoms **517**, 49 (2022), doi:10.1016/j.nimb.2022.02.012.

[13] W. Eckstein, *Computer simulation of ion-solid interactions*, vol. 10, p. 176, Springer series in materials science (2013).

[14] Z. Chen *et al.*, *Dynamic Monte Carlo simulation for reactive sputtering of aluminium*, Nuclear Instruments and Methods in Physics Research Section B: Beam Interactions with Materials and Atoms **207**(4), 415 (2003), doi:10.1016/S0168-583X(03)01120-0.

[15] X. Lin *et al.*, *Gold carbide: A predicted nanotube candidate from first principle*, Nanomaterials **11**(12), 3182 (2021), doi:10.3390/nano11123182.

[16] A. Palenzona *et al.*, *The heat of formation of the YbAl2 compound*, Thermochimica Acta **23**(2), 393 (1978), doi:10.1016/0040-6031(78)85084-9.

[17] J. E. Saal *et al.*, *Materials design and discovery with high-throughput density functional theory: the open quantum materials database (OQMD)*, JOM **65**, 1501 (2013), doi:10.1007/s11837-013-0755-4.

[18] S. Kirklin *et al.*, *The open quantum materials database (OQMD): assessing the accuracy of DFT formation energies*, npj Computational Materials **1** (2015), doi:10.1038/npjcompumats.2015.10.

[19] T. E. Cocolios *et al.*, *The institute for nuclear and radiation physics at the university of leuven*, Nuclear Physics News **27**(4), 18 (2017), doi:10.1080/10619127.2017.1317178.

[20] M. Mayer, *Simnra user's guide* (1997).

[21] J. Evertsson *et al.*, *The thickness of native oxides on aluminum alloys and single crystals*, Applied Surface Science **349**, 826 (2015), doi:10.1016/j.apsusc.2015.05.043.

[22] J. Zuo and A. Erbe, *Optical and electronic properties of native zinc oxide films on polycrystalline Zn*, Physical Chemistry Chemical Physics **12**(37), 11467 (2010), doi:10.1039/C004532B.

[23] U. Kentsch, *40 kV ion implanter*, https://www.hzdr.de/db/Cms?pOid=41438&pNid=923 (2024).